# Regioselective cleavage of aryl ether C–O bond rationalised from the carburization degree of tungsten carbides

Huihuang Fang[1], Alberto Roldan[2]*, Yanping Zheng[1], Chenchen Tian[1], Xinping Duan[1], Kun Chen[1], Linmin Ye[1], Stefano Leoni[2], Youzhu Yuan[1]*

[1] *State Key Laboratory of Physical Chemistry of Solid Surfaces, National Engineering Laboratory for Green Chemical Productions of Alcohols-Ethers-Esters and iChEM, College of Chemistry and Chemical Engineering, Xiamen University, Xiamen, 361005, China*

[2] *School of Chemistry, Cardiff University, Main Building, Park Place, Cardiff, CF10 3AT, United Kingdom*

* To whom correspondence should be addressed.

E-mail: RoldanMartinezA@cardiff.ac.uk, yzyuan@xmu.edu.cn

**Abstract**

Tungsten carbides display excellent performance in many heterogeneously processes because of their “Pt-like” catalytic properties. Preparation of tungsten carbides with controllable phase composition intently relevant to their catalytic behaviors is essential yet challenging. In this study, a structure-tuning tungsten carbide embedding in the carbon spheres ($W_xC$@CS) was fabricated via carburization of organic-inorganic hybrid precursors, exhibiting high activity and promising regioselectivity towards C–O bond hydrogenolysis. The rational tuning of the structure of $W_xC$@CS was explored intensively. The catalytic hydrogenolysis performance is compared with those of a commercial-available WC transforming from inert phase to a composition-dependence active catalyst by structure reconstruction. The combined catalytic and characteristic analysis illustrates that the phenol production was dependent on the C-defect sites. Subsequently, an intimate connection between the phenol yield and the C/W atomic ratio on the exterior interface of the catalyst were verified. The C/W atomic ratio of 7.2 gives the optimal catalytic performance. Density functional theory (DFT) calculations were performed to define the catalytic mechanism at an atomic level. This theoretical analysis suggests an appropriate configuration of surface W and C atoms for activation of dihydrogen and guaiacol molecular, rendering the intrinsic active sites for phenol production. This work sheds light on controlling the surface compositions of tungsten carbides for an efficient C–O bond cleavage catalysts.

**Keywords:** Tungsten carbide; Guaiacol; Hydrogenolysis; C–O Bond cleavage; Phenol; Regioselectivity

## 1. Introduction

Transition metal carbides (TMCs) have triggered substantial attention as potential catalytic materials in heterogeneous catalysis due to their distinctive "Pt-like" catalytic behaviors in various significant reactions [1],[2],[3],[4],[5],[6],[7],[8]. The insertion of carbon atoms into the parent transition metals induces a rearrangement, which results in their transformation of steric and electronic properties. These changes contribute to the formation of bonds with certain covalent character and charge transfer between metal and carbon atoms leading to TMCs (e.g., tungsten carbides and molybdenum carbides) [2],[9],[10]. Theoretical studies have indicated that the presence of carbon in the lattice of parent metal promotes a significant redistribution of the density of states, affording them with a higher d-band electronic density of states at the Fermi level, and thus affecting their catalytic performance [6],[11],[12]. Importantly, the formation of TMCs, carbon diffusion and carburization control are of particular importance for designing efficient TMC catalysts capable of dominating catalytic behaviors, distinguishing from their parent metal [13].

As typical TMCs, tungsten carbides have demonstrated encouraging catalytic performance in hydrogenolysis, hydrogenation, isomerization, deoxygenation, and more recently, $H_2$ evolution reactions (HER) [3],[4],[5],[6],[7][14],[15],[16],[17]. Bitter and co-workers [3],[4],[7],[16] advocated $W_2C$-based catalysts for efficient deoxygenation of oxygen-rich biomass-derived feeds including stearic acid, oleic acid, and guaiacol, producing a high yield of hydrocarbons and phenolics. Previous reports showed WC monocarbides possess HER activity enabling them as promising candidates to catalyze such reaction [18],[19]. Recently, Gong et al. [6] synthesized phase-pure $W_2C$ nanoparticles supported on carbon nanotubes that displayed impressive HER performance superior to those of WC materials. The difference in their activities are relying on the carburization control by which different carbide phases with C-defect sites is tuned. However, it receives far less attention on the structure-activity relationship mainly due to the complexity of carbide phases involved to phase purity, surface defects, surface carbon, surface termination and surface oxides [20],[21]. To this end, the needed control of the carbide phase formulation and the elucidation of relationship between catalytic behavior and structures are particularly important yet challenging.

The critical issue is the accurate synthesis of TMCs with control of the carbon diffusion process, which facilitates the identification of phase formulation and surface compositions. Previous reports have shown that the protocols to synthesize TMCs is typically by temperature-programmed reduction (TPR) using gaseous carbon precursors such as $CH_4$, $C_3H_8$ or CO [22],[23],[24],[25]. In this way, the carbon diffusion is fast through the gas-solid interface and barely modulable, which results in the uncontrollability of the phase composition, i.e. C-defects on the carbide catalysts. To solve this problem, carbothermal hydrogen reduction was developed and applied using solid carbon as controllable carbon sources during pyrolysis [3],[6],[14],[15],[26],[27],[28]. This method speeds down the carbon diffusion through the solid-solid interface, avoiding excessive carbon deposition and making it easy to tune the phase composition. Various carbon materials, such as activated carbon, carbon nanotubes, and carbon fibers were adopted as carbon sources for the production of metal carbides [3],[6],[15]. In addition, Xu and Wu et al. [27],[28] employed metal-organic frameworks as precursors and synthesized metal carbide nanoparticles by pyrolysis and carbon diffusion. Indeed, we have prepared tungsten carbides with well-defined phase composition by controlling the carburization level of phenolic polymers in the presence of tungsten precursors. The obtained tungsten carbide catalysts revealed promising performance for selective hydrogenolysis of aryl ether C–O bonds [14], of particular importance connecting the conversion and valorisation of oxygen-rich lignocellulosic biomass [14],[29],[30],[31]. This method for synthetizing carbides displays significant advances in the fabrication and control of structural phases. However, the identification of reactive phase, role of C-defects on metal surroundings, and structure-activity relationship are not yet clear.

In this work, tungsten carbides with different phase formulations were fabricated and applied to catalyze the hydrogenolysis of guaiacol revealing its capability to cleavage C–O bonds and to elucidate the role of active C-defect sites. The catalysts synthetized and their activity were characterized in detail using various techniques, including X-ray diffraction (XRD), X-ray photoelectron spectroscopy (XPS), high-sensitivity low-energy ion scattering spectroscopy (HS-LEIS), transmission electron microscopy (TEM), temperature programmed desorption (TPD) and first density functional (DFT) calculations. The optimal $W_xC$@CS displays high activity for phenol production, which is attributed to surface configuration and

variation of electronic properties through appropriate carburization control. Controlled experiments by reconstruction of commercial-available tungsten carbides were conducted for further evidence. A correlation between the phenol STY (space time yield) and the surface C/W atomic ratio was established and the plausible scheme of guaiacol hydrogenolysis was proposed.

## 2. Experimental

### 2.1 Synthesis of materials

Tungsten carbides ($W_xC_y$-NPs@CS, CS: carbon spheres) were synthesized by carburization of organic-inorganic hybrid precursors [14]. Briefly, 5.0 g meta-tungstate and 1.2 g resorcinol were dissolved in deionized water with continuous stirring for 30 min; 2.3 mL formaldehyde was slowly added and the mixed solution was heated to reflux at 85 °C for 24 h, followed by the formation yellow powder precursors. The precursors with washing and drying treatment were carburized at desired temperature under $H_2$. Typically, W@CS was prepared by carburizing at 700 °C for 2 h with a heating rate of 5 °C/min. $W_2C$@CS was carefully carburized at 800 °C at a heating rate of 1 °C/min for 30 min. $W_xC$@CS and WC@CS were carburized at 850 °C at a heating rate of 3 °C/min for 3 h and 6h, respectively. Prior to exposure to air, the as-prepared samples were passivated by 1%$O_2$/99%$N_2$ for 30 min.

Commercial-available WC (denoted as Com-WC) samples with different surface reconstructions were prepared by following methods. Com-WC was obtained from Aladdin Co. Ltd. In brief, 1 g of Com-WC and 240 mg $WCl_6$ were dispersed in 100 ml ethanol with continuous stirring for 30 min. 4 mL water was slowly added and the temperature of solution was heated to and maintained at 80 °C overnight. The obtained solid was filtered, washed several times and vacuum drying. W-Com-WC pretreated at 450 °C for 4 h at a rate of 5 °C/min under $H_2$. $W_{1+x}C$-Com-WC was first pretreated from 20 to 450 °C at a rate of 5 °C/min under $H_2$; then 450 to 750 °C at a rate of 1 °C/min for 1 h under 15% $CH_4/H_2$. C-defect $W_xC$-Com-WC samples with different surface C/W atomic ratio were first pretreated similar treatment under $H_2$; then 450 to 750 °C at a rate of 1 °C/min for 0-6 h under 15% $CH_4/H_2$. The surface C/W atomic ratio were calculated from the HS-LEIS results.

$WO_3$-Com-WC was pretreated at 450 ºC for 4 h at a rate of 5 °C/min under Ar. The similar passivated treatments with preparation of $W_xC_y$-NPs@CS were conducted prior to exposure to air.

2.2 Activity test

The catalytic activity for guaiacol hydrogenolysis was performed on a fix-bed reactor with a computer-controlled auto-sampling system. In brief, 200 mg of fresh catalyst was loaded in the centre of quartz tubular reactor sandwiched with quartz powers. Before test, the catalysts were pretreated at 450 °C for 4 h under 5%$H_2/N_2$ with a heating rate of 3 °C/min. The catalyst bed was cooled naturally to target temperature, and pure $H_2$ gas was fed into the reactor as the pressure of 3.0 MPa. Subsequently, liquid guaiacol was pumped into the reactor by a Series III digital HPLC pump (Scientific Systems, Inc.) with required weight liquid hourly space velocity (WLHSV). The products were analyzed on-line using an Agilent 7890A gas chromatograph (GC) equipped with an auto-sampling value, flame ionization detector (FID) and a DB-Wax capillary column. A GC 2060 with thermal conductivity detector and a TDX column was used for the analysis of gas products ($CH_4$, CO, $CO_2$, and $H_2O$). The details for calculation of guaiacol conversion and product selectivity are available from our previous reports [14,29]. The apparent activation energy was obtained by the Arrhenius equation on the condition that the conversion was below 40%.

2.3 Materials characterization

XRD analysis was conducted by a Rigaku Ultima IV X-ray diffractometer equipped with a Cu–$K_\alpha$ radiation (35 kV and 15 mA) at scanning 2θ from 10° to 90°. The obtained diffraction data were analyzed by using the JCPDS database. The XRD Rietveld refinement was carried out using Topas software to calculate the W/$W_2C$/WC weight ratio.

A scanning electron microscopy (SEM, Hitachi S4800) was used for observation of the morphology of samples.

TEM, HR-TEM and HAADF-STEM images were obtained by a Philips Analytical FEI Tecnai 30 electron microscope operated at an acceleration voltage of 300 kV. The fresh samples were dispersed ultrasonically and then dropped and dried on copper grid with lacey

support films.

XPS measurements were conducted on an Omicron Sphera II photoelectron spectrometer equipped with an Al–$K_\alpha$ X-ray radiation source (hν= 1486.6 eV). The binding energy was calibrated using the C 1s peak at 284.5 eV. HS-LEIS spectra were obtained by an Ion-TOF Qtac100 instrument. In order to gain the surface information and minimize the surface damage, He was selected as the ion source at a kinetic energy of 3keV with ion flux of 6000 pA $m^{-2}$ and a spot size of 2000 um × 2000 um.

CO and $H_2$-TPD measurements were carried out by a Micromeritics AutoChem II 2920 chemisorption analyzer. 200 mg of the sample was used in each test. Before test, the sample was in situ pretreated under the similar condition with that of the activity evaluation of catalysts. Ar gas was introduced to clean the surface of the sample for 1 h at 400 °C. Then the sample was cooled down at room temperature, followed by switching $H_2$ or CO stream for adsorption for 1 h. Afterwards, the sample was flushed by Ar till a stable baseline. TPD measurements were operated from 30 °C to 500 °C with a ramping rate of 5 °C/min. The desorbed exit-gases were monitored by a thermal conductivity detector.

2.4 Computational details

Periodic plane-wave DFT calculations were performed using the Vienna ab-initio simulation package (VASP) [32],[33], the open-shell Perdew–Burke–Ernzerhof functional [34] and kinetic energy of 550 eV to expand the plane-waves of the Kohn-Sham valence states [35]. The inner electrons were represented by the projector-augmented wave (PAW) pseudopotentials considering also non-spherical contributions from the gradient corrections [36]. All the calculations include the long-range dispersion correction approach by Grimme (D3) [37], which is an improvement on pure DFT when considering large polarizable atoms [38],[39],[40]. The optimisation thresholds were $10^{-5}$ eV and 0.01 eV/Å for electronic and ionic relaxation, respectively. The Brillouin zone was sampled by Γ-centred k-point mesh generated through a Monkhorst-Pack grid [41] with a maximum separation of 0.20 $Å^{-1}$between **k**-points, which ensures the electronic and ionic convergence. The

electronic partial occupancies were determined using the tetrahedron method with Blöchl corrections to increase the integration efficiency for all the calculations [42].

The $W_2C$ bulk (crystal symmetries P-31m) volume, shape and internal coordinates were optimised leading to cell parameters a= b= 5.190 Å and c= 4.724 Å forming an angle of 120.0° in full agreement with an experimental benchmark (a= b= 5.208 Å and c= 4.737 Å) [43]. The bulk of WC has a crystal symmetry P-6m2 and upon relaxation within the computational setup remained in the same symmetry and with cell parameters of a= b= 2.906 Å and c= 2.838 Å, wich are also in excellent agreement with crystallographic data (a= b= 2.904 Å and c= 2.383 Å) [44].

We have simulated the low-Miller index surfaces considering the different terminations, i.e. carbon and tungsten, as in slab models. The slab models were built following the dipole method, which is based on the condition that the net dipole perpendicular to the surface must be zero, as determined by Tasker [45]. All the surfaces studied were generated by cutting the optimized bulk of the iron minerals using the METADISE code [46]. We added a vacuum width of 15 Å between vertically repeated slabs, to avoid spurious interaction between them. These slabs models contain enough atomic layers to allow the uppermost five layers to be completely relaxed without symmetry restrictions and the bottom ones were frozen at the bulk lattice parameter. **Table S1** contains a summary of areas and surface energies calculated according to **equation 1**, for each slab investigated. The surface energy ($\gamma$), which measures the excess of energy of the surface with respect to the bulk, has been calculated as

$$\gamma = \frac{E_{slab} - nE_{bulk}}{A} - \frac{E_{slab}^{unrelaxed} - nE_{bulk}}{2A} \quad (\mathbf{1})$$

where $E_{slab}$ is the absolute energy of the relaxed slab, $E_{slab}^{unrelaxed}$ is the energy of surface slab where the atoms are frozen at their bulk positions, $E_{bulk}$ is the energy of a carbide's bulk, $n$ is the number of stoichiometric units in the surface cell and $A$ is the surface area.

## 3. Results and discussion

### 3.1 Preparation of catalysts with controllable phase composition

The $W_xC_y$-NPs@CS catalysts were synthesized by carburization of organic-inorganic

hybrid precursors over specific heating rate, carrier-gas flow and carburizing time. **Scheme 1** shows the evolution of crystalline phase under the carburization treatment [14]. Metal W NPs were generated through the carbothermal hydrogen reduction at the first stage; then the diffusion of interstitial carbon atoms into the reduced metal W promoted the formation of the $W_2C$ phase. Furtherly, deeper carburization formed the WC crystalline phase with the content of $W_2C$ declined gradually. We identified the crystallinity and phase purity comparing with XRD patterns (**Fig. S1**). The formation of various crystalline phases depends on the control of carburizing conditions. The sharp diffraction peaks centred at 2θ of 40.42°, 58.36°, and 73.33° display the high crystallinity of metal W (PDF#04-0806), as depicted in W@CS. In contrast, $W_2C$@CS exhibits distinctive peaks located at 34.47°, 38.10° and 39.67°, which are indexed to the (100), (002) and (101) of facets of $W_2C$ (PDF#65-3896), respectively. $W_2C$ has a hexagonal structure (P-31m) with lower C composition while WC contains a hexagonal structure of P-6m2 whereas the C planes are sandwiched between tungsten layers. With deeper carburization, typical peaks centered at 31.70°, 35.89° and 48.65° are visible in $W_xC$@CS, revealing the generation of WC (PDF#65-4539). The XRD pattern in WC@CS obtained well-crystallized WC phase without any $W_2C$ or metal W phase, indicating complete carburization. For further analysis, **Table S2** shows the identification of phase composition by XRD Rietveld refinement and other physicochemical properties; see Section 2 for details on the preparation and characterization process.

In order, W@CS, $W_2C$@CS, and WC@CS, with an optimal $W_xC$@CS, were readily fabricated through the method state above. It is worth to note that the phase evolution of tungsten carbides affects the structural and electronic properties, and hence the catalytic performance. In this case, the phase composition can be designed rationally through optimizing the carburization level, which may facilitate seeking promising active phases for a wider catalytic application.

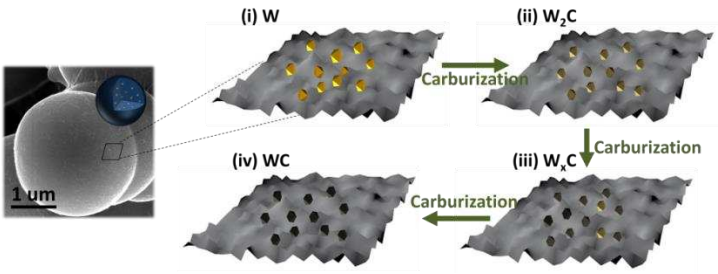

**Scheme 1** Evolution of crystalline phase under carburization of precursors.

To model the catalysts' surfaces, we selected the lowest in surface energy, i.e. $W_2C${101} and WC{110}, which are also in agreement with the XRD data. We build several structures decreasing the C/W ratio from the pristine WC{110} to 0.88 considering different carbon vacancies, i.e. top and subsurface carbons, as well as scattered and contiguous positions. Their relative stability is expressed in **Fig. S2**, where the relative energy (ΔE) considers the species' chemical potential as the unity. Hence, ΔE is defined as the energy difference between the vacancy system plus the number of carbons (as in graphite) and the pristine WC{110}. It shows that any C-vacancy above a C/W ratio of 0.918 is more stable at the top atomic layer whereas below that ratio, the vacancy will be at the subsurface. We simulated a $W_xC$ structure with C/W ratio of 62.5 % in agreement with the reconstructed $W_{1+x}C$ surface ratio.

3.2 Catalytic performance

The catalytic conversion of guaiacol involves the cleavage of diverse C−O bonds and the hydrogenation of arene species. We selected this reaction as a model, aiming at elucidating the active sites of the catalysts and understanding the structure-activity relationship. **Scheme S1** shows two competitive pathways on guaiacol conversion: one involves the hydrogenation of the aromatic ring to alkylated cyclohexanols, followed by the cleavage of aliphatic C−O bonds to cyclohexane, which usually take place on noble metals such as Pt and Ru (dash line) [47],[48]; the other mechanisms encompasses the direct hydrogenolysis of C−O bonds to give phenols, which may be then overhydrogenated into corresponding cyclohexanol and cyclohexane (dark line) [7,14,29].

As shown in **Fig. 1**, the W-based catalysts show preferences on the hydrogenolysis of C−O bonds without arene hydrogenation. W@CS presents a 28.2% guaiacol conversion via cleavage of aliphatic $CH_3$−O bonds, producing 56.7% of catechol selectivity. In contrast, the $W_2C$@CS shows the high conversion of 83.6% towards phenol, anisole, and benzene, indicating a great capability for hydrogenolysis of aryl C−O bonds with poor selectivity. The optimal $W_xC$@CS catalyst exhibits the highest conversion of 98.6% with 91.5% phenol

selectivity, exhibiting a regioselective cleavage of $C_{aryl}$–$OCH_3$ bond. Absolute carburization over the WC@CS catalyst caused the rapid decline of activity, obtaining only 30.1% guaiacol conversion and 70.7% phenol selectivity. To investigate the effect of structure transformation on the catalytic performance, controlled experiments were conducted by physical mixture of $W_2C$@CS and WC@CS as a contrastive catalyst. The mixed catalysts showed poorer performance (11.5% and 73.7% selectivities of anisole and phenol, respectively), even when the catalysts contained a similar amount of $W_2C$ and WC than the original $W_xC$@CS catalyst.

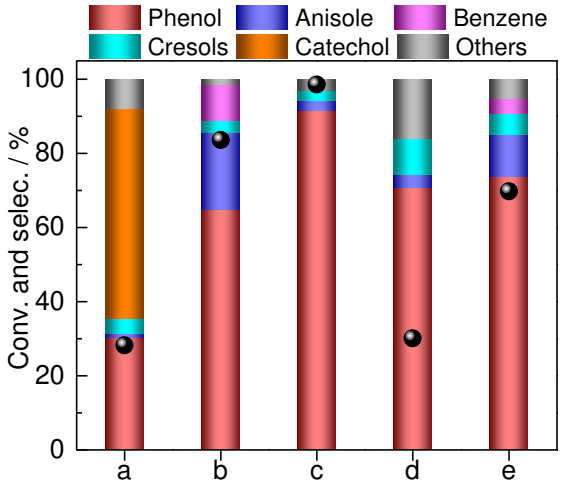


**Fig. 1** Catalytic performance for guaiacol conversion (black dot) over tungsten carbide catalysts with different phase composition: (a) W@CS, (b) $W_2C$@CS, (c) $W_xC$@CS, (d) WC@CS, (e) Physically mixed $W_2C$@CS and WC@CS with the similar phase composition with $W_xC$@CS. Reaction conditions: weight liquid hourly space velocity (WLHSV) = 3.0 $h^{-1}$, P ($H_2$) = 3.0 MPa, $H_2$/GUA molar ratio = 50, T= 300 °C.

The apparent activation energy (Ea) is a critical parameter directly related to the performance of the catalysts. We used the Arrhenius plots to derive the Ea for guaiacol conversion (**Fig. 2**). Ea was 189.7 kJ/mol for W@CS, much higher than those found for tungsten carbides. Notably, $W_2C$@CS displays a quite low Ea value of 111.1 kJ/mol compare to the other W-based catalysts considered here. In fact, the Ea increases with the catalysts' carburization up to a constant of approximately 150.0 kJ/mol. Thus, $W_2C$ performs the cleavage of C–O bonds faster than WC but with poor regioselectivity. $W_xC$@CS has a moderate Ea value of 145.5 kJ/mol and displays the highest phenol selectivity. That is to say,

suitable Ea promotes the regioselective cleavage of $C_{aryl}$–$OCH_3$ bond. This difference in Ea is most likely caused by difference in the structure and C-defects and appropriate carbon diffusion to parent tungsten, is essential for controlling the regioselective hydrogenolysis of guaiacol to phenol.

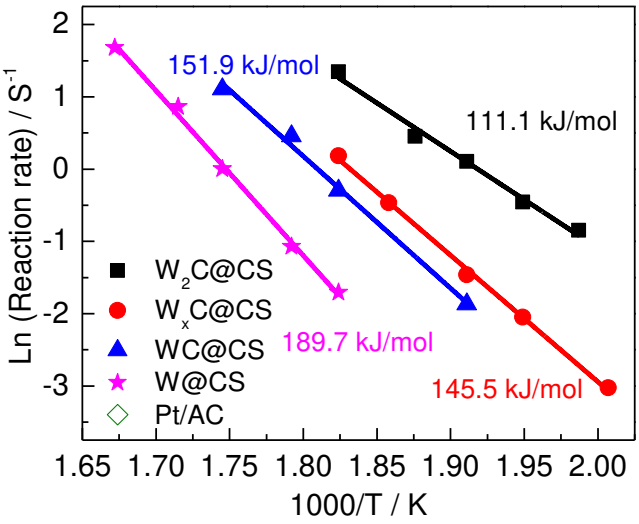


**Fig. 2** Arrhenius plots of the reaction rate (ln(r)) versus 1/T for the GUA conversion over W-based catalysts and 5%Pt/AC.

We explored different adsorption sites following standard simulation methods and found the different interaction strength between molecules and catalysts. Overall, the adsorption energies of the different species is stronger on $W_2C$, followed by WC and $W_{1.25}C$, see **Table 1**. On $W_2C$, the adsorption of phenol is stronger than any other species investigated, which may explain yields on further hydrogenated species, e.g. benzene. This is not the case of $W_{1.25}C$ and WC, which adsorption energies become weaker with the degree of hydrogenation. The strength of these interaction is expressed also on the distances between the molecule and the surface, see **Table 1**. Furthermore, the adsorption energies and distances relates well with the charge transfer from the surface to the molecule. The charge transferred on $W_2C$ (~0.7 e) is more than twice this on WC (~0.3 e), and much bigger than on $W_{1.25}C$ (~0.1 e). The charge transferred does not directly correlates with the surface's work function, i.e. 4.2, 4.13 and 4.53 eV respectively for $W_2C$, $W_{1.25}C$ and WC, which indicates that the redox properties of the catalysts does not control the process. A part from a not so strong adsorption energy with

limited electron transfer to the molecule, we could not identified any other clear trend between the electronic and geometric structure with the catalytic activity.

**Table 1**. Summary of adsorption energies ($E_{ads}$) and average distance between the molecules and the surfaces ($d_{molecule-surface}$) on the $W_2C$, $W_{1.25}C$ and WC surfaces.

| | $E_{ads}$ (eV) | | | $d_{molecule-surface}$ (Å) | | |
|---|---|---|---|---|---|---|
| | $W_2C$ | $W_{1.25}C$ | WC | $W_2C$ | $W_{1.25}C$ | WC |
| Guaiacol | -3.04 | -2.11 | -2.43 | 2.60 | 2.72 | 2.75 |
| Catechol | -2.68 | -1.76 | -2.37 | 2.44 | 2.60 | 2.72 |
| Anisole | -2.70 | -1.80 | -2.39 | 2.58 | 2.84 | 2.88 |
| Phenol | -3.33 | -1.64 | -2.10 | 2.23 | 2.70 | 2.56 |
| Benzene | -2.23 | -1.05 | -2.07 | 2.33 | 2.82 | 2.70 |

3.3 Texture feature, electronic property and chemisorption behaviour of the catalysts

TEM measurements were employed to gain more detailed information about the textural structure. The samples with different carburization show similar morphologies, see **Fig. S3**. The carbide nanoparticles are formed and evenly embedded in carbon spheres with average diameters of 4-10 nm. Taking $W_xC$@CS nanoparticles as representatives, the HR-TEM analyses were demonstrated in **Fig. 3**. **Fig. 3a** exhibits clear lattice fringes with interplanar distances of 0.227 nm, 0.259 nm, 0.188 nm and 0.252 nm, corresponding to the (101), (100) facets of $W_2C$ and WC, respectively. In addition, the Fast Fourier transform (FFT) images of given regions in blue and yellow rectangle (**Fig. 3b and c**) were also analyzed and the results manifest the (h k l) planes ascribed to the diffractions of $W_2C$ (blue rectangle) and WC (yellow rectangle) facets, which indicates the coexistence of different crystallographic planes. For more evidence, a set of seven interplanar spacings, marked by double-headed arrow in **Fig. 3a**, were carefully measured and the results shown in **Fig. 3d and e**. The distance of region i and ii are 1.589 and 1.762 nm, owing to the $W_2C$ (101) and WC (100) facets. More interestingly, many dark spots are observed (marked by white arrows) in these carbide nanoparticles (**Fig. 3f-h**); these spots are ascribed to the C vacancies on the surface of nanoparticles, in agreement with previous reports [17]. It is well-known that, vacancies can be regarded as volume defects and they are capable of trapping and activating reactants. These results reveal a transformation of diverse crystal defects with C-defect sites by using the carburization of organic-inorganic hybrid precursors.

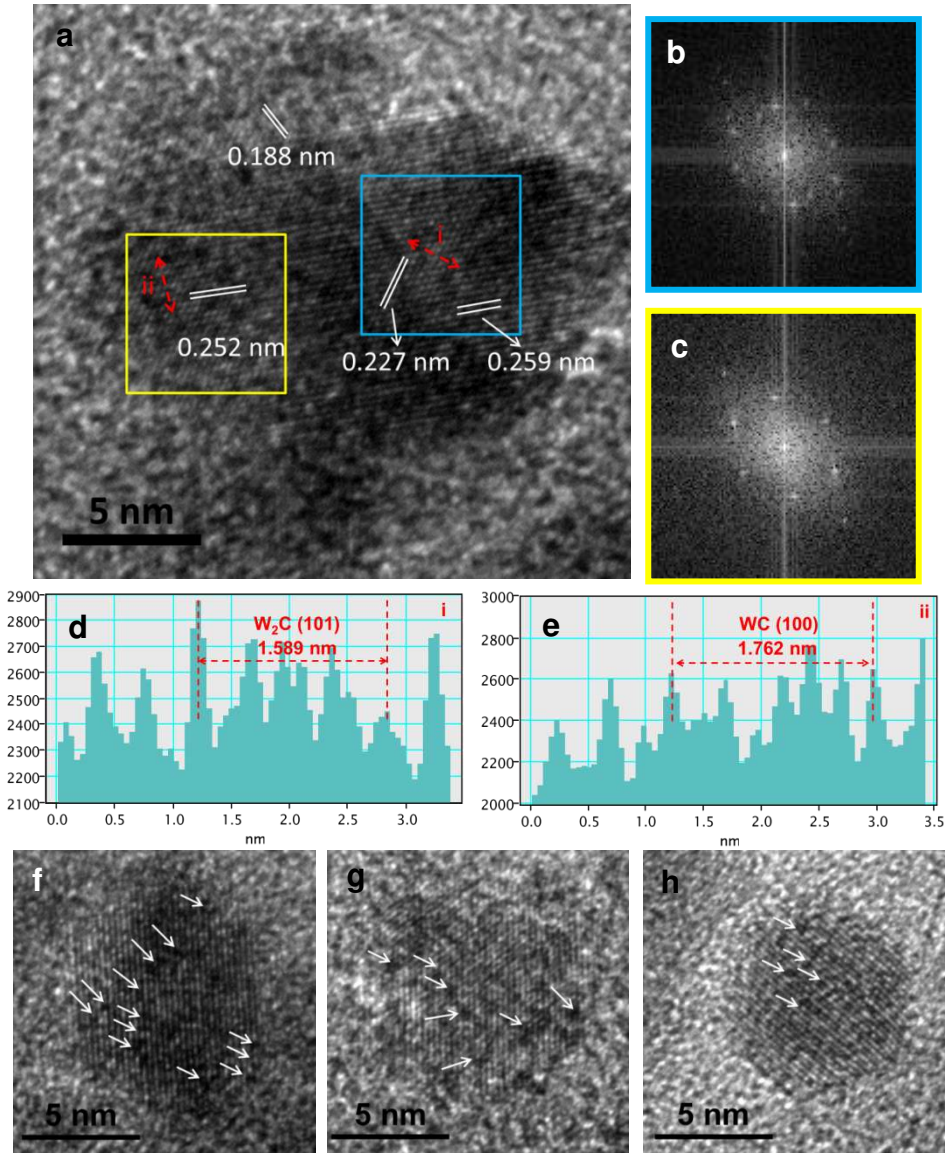


**Fig. 3** HRTEM image of samples: (a, g) $W_xC$@CS; (f) $W_2C$@CS; (h) WC@CS; the white arrows show C vacancies in carbide crystallites. (b, c) Fast Fourier transform (FFT) images of given regions in blue and yellow rectangle, respectively. (d, e) The measured d spacing of nanostructured units marked by double-headed arrow; and i-ii reveal 7 interplanar spacing in different regions taken from (a).

To this end, XPS analyses were carried out and the results are shown in **Fig. 4** and **Table S3**. As indicated from the deconvoluted W 4f spectrum in **Fig. 4a**, W@CS was featured with two peaks at 29.1 and 31.2 eV ascribed to the metal W; this implies that metallic W is the majority species in the W@CS catalyst. In contrast, two characteristic carbidic peaks appear

in tungsten carbide samples. The $W_2C$@CS displays two pronounced peaks centered at 31.4 and 33.7 eV corresponding to the tungsten carbide species. A tiny peak assigned to metallic W still exists, presumably due to slight lack of carbon atoms on the surface. Moreover, the binding energy of W 4f is shifted from 31.4 to 31.9 eV with deeper carburization. In parallel, as a consequence of surface passivation during the catalysts preparation, the peaks assigned to oxides (35.3 and 37.5 eV) were inevitable on the surface of all samples. Indeed, the d-band of the electronic density of states (DOS) derived from our computer models show a shift of the occupied d-band centre of 0.30 eV as a function of the carbonization level (**Fig. S4**). The higher binding energy found in the XPS implies that W provides electrons to C species resulting in a greater accumulation of electron density around C. This was also probed as evidence in **Fig. 4b**. The deconvolution of C 1s energy level signals revealed two peaks, which were ascribed to graphitic and carbidic species. The peak located at 284.5 eV belongs to the graphitic C and is unchanged during the carburization. However, the carbidic peak firstly centered at 282.1 eV in $W_2C$@CS and then shifted to lower binding energy of 281.2 eV in WC@CS with increasing carburization. The change in binding energies suggested that the carburization control is of particularly importance and results in charge transfer between W and C.

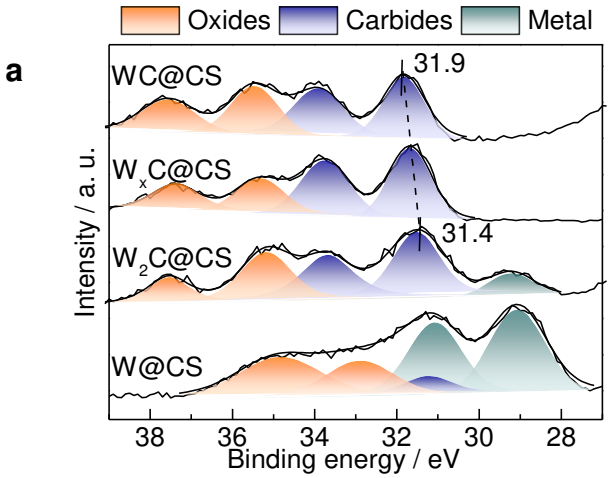

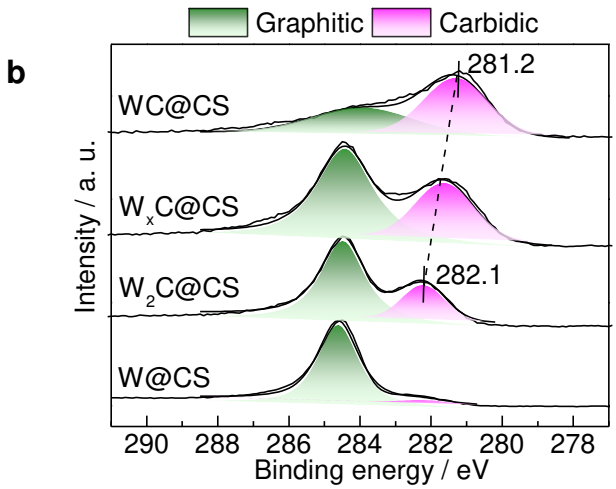


**Fig. 4** XPS profiles of W-based catalysts: (a) W 4f and (b) C 1s.

A set of typical TPD measurements were carried out to gain insight into the chemisorption behaviors. Carbon monoxide (CO) is a typical probe molecule to investigate the relative electron donating and accepting capability of the reactants as well as surface reactive sites of heterogeneous catalysts [8,49]. Lee et al. [8] studied CO chemical titration to determine the reactive sites in $Mo_2C$-catalyzed anisole hydrodeoxygenation. They have found that the benzene synthesis rate remarkably declined in the presence of CO and they could be restored through removal of CO, indicating the CO reversible poisoning of the reactive sites activating substrates. In our case, CO-TPD was performed to provide further evidence of the W–C electron relocation as a function of the carburisation degree, as indicated in **Fig. 5a**. On the W@CS sample, CO desorbs as two large broad peaks at 83 °C and 149 °C. Theoretical studies have shown that CO bonding with C end down was favored on the metallic sites which provide a greater electron donation, leading to a higher desorption energy [10]. Unlike W@CS, carbidic species ($W_2C$@CS, $W_xC$@CS and WC@CS) display weaker absorption. With deeper carburization, the CO desorption peaks shifted to lower temperatures from 83 °C to 70 °C and 149 °C to 132 °C, respectively. The two broad desorption peaks were narrowed and divided in two more obvious peaks in $W_xC$@CS, indicating the existence of two active sites. Interestingly, the WC@CS display only a lower desorption peak probably due to the complete formation of WC. The weaker CO absorption on carbides indicates lower electronic density on the metallic sites existed on the carbide surface; this is also proved from the XPS analysis.

It is also important to investigate the absorption behavior of hydrogen when it comes to the $H_2$-related reactions such as hydrogenolysis. As shown in **Fig. 5b**, two broad hydrogen desorption peaks could be recognized in these samples. W@CS shows smaller and weaker hydrogen desorption peaks than those of carbides and the major peak was located at 76 °C. While $W_2C$@CS and $W_xC$@CS display large peaks centered at 89 °C with a more obvious shoulder peak at higher temperature of 120°C. With absolute carburization, WC@CS showed a slight decrease on the amount of hydrogen desorption. These results reveal that carbides were bonding strongly with hydrogen, affording more disassociated and absorbed hydrogen on the carbide surface. DFT calculations and experiments have shown that hydrogen can be activated, adsorbed and bonded to the hollow sites on the surface of metal carbides and the increase of the d-band density of states caused by the insertion of carbon atoms is also beneficial for hydrogen activation [10,50,51]. The difference on the chemisorption behaviors imply that the C-defect sites can be tuned by carburizing level, in agreement with TEM analyses mentioned above. As a matter of fact, the CO-TPD and $H_2$-TPD results correlated well that weaker CO absorbed sites and more H-occupied hollow sites existed on the surface of carbides. Therefore, a suitable carburization of the catalysts offers an appropriated activation of reactants.

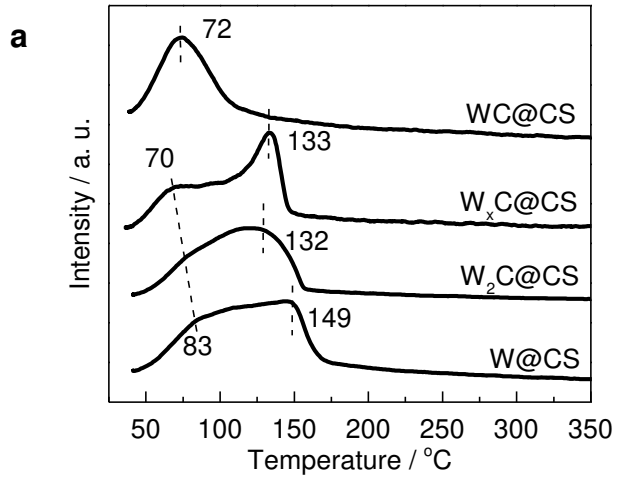

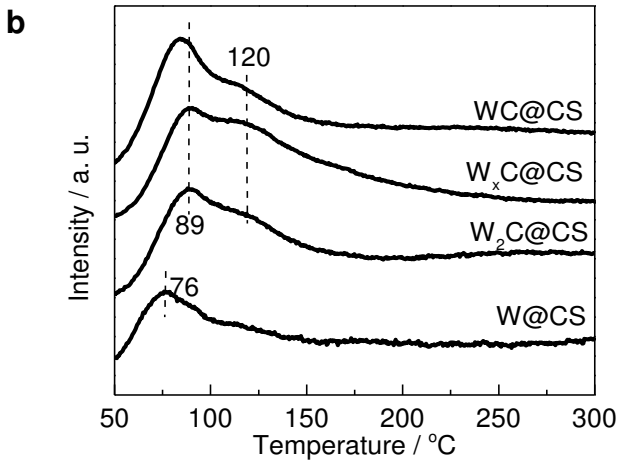


**Fig. 5** TPD spectra of CO (a) and hydrogen (b) desorption over W-based catalysts.

3.4 Reconstruction of the active phase and understanding of the origin of catalytic performance

To exclude the effect of supported carbon and gain insight into the catalytic origin on the surface configuration, reconstruction methods on the Com-WC were carried out to provide further experimental evidence. No residual carbon was detected in Com-WC sample from the Raman spectra (**Fig. S5**). To create C-defect surfaces, tungsten precursors were deposited onto the surface of Com-WC by hydrolysis of $WCl_6$, and then a careful carburization control was furtherly employed for formation of $W_{1+x}C$ phase on the surface. For comparison, Com-WC modified with other tungsten species were also prepared, see Section 2 for details. The XRD patterns of samples were employed to investigate the crystallinity and phase composition, as illustrated in **Fig. S6**. Specifically, the precursor with a careful carburization displays two typical peaks of $W_{1+x}C$ species by insufficient insertion of carbon atoms, revealing successful modification with more C-defect sites on the surface, namely $W_{1+x}C$-Com-WC.

Typical morphologies of Com-WC and $W_{1+x}C$-Com-WC were identified using SEM, TEM, HAADF and HR-TEM measurements. As indicated in **Fig. S7**, large Com-WC bulks were observed clearly with smooth surfaces, while became rougher with rich stacking faults after modification revealing the successful deposition of a non-continuous carbide phase. Structurally, Com-WC possesses bare lattice fringe with an interplanar distance of 0.188 nm, fitting with the typical (101) facets of WC (**Fig. 6a**). In contrast, as sketched from the **Fig. 6b**,

$W_{1+x}C$-Com-WC provides grain lattice facets, stacking faults and C-defect sites. Clear lattice fringes of 0.227 and 0.249 nm corresponding to the (101) facet of $W_2C$ and the (100) facet of WC have newly emerged; the lattice fringes ascribed to $W_2C$ and WC locate at the same region (yellow rectangle) reveal a coexistence of different crystallographic planes. These diverse facets expose different crystal defects and cause the formation of stacking faults and boundaries, leading to the atom dislocation and distinct configuration between W and C atoms. A lattice fringe of 0.156 nm in red rectangle is visible, which is attributed to (200) facet of W presumably due to the uncompleted carburization. The FFT images of given regions in red, blue and yellow rectangles also confirm the diffractions of the (h k l) planes over these species. Most interestingly, it was found that $W_{1+x}C$-Com-WC contained large amount of C vacancies marked by white arrows, indicating the formation of hollow active sites, which favor the activation of hydrogen and substrates. That is to say, the reconstruction of carbide surface with abundant dislocations and crystal defects was successfully achieved.

The catalytic performance for guaiacol hydrogenolysis was evaluated to investigate the effect of these distinct modifications on the Com-WC, as demonstrated in **Table 2**. Com-WC without any modification displayed negligible activity. In comparison, the activities changed in variety after different modification. W-Com-WC performed a slightly increased conversion with high selectivity of catechol. This reveals that the incorporation of metal W overlap the hollow carbidic sites for the activation of hydrogen and is likely to strengthen the absorption of guaiacol, resulting in catechol production via cleavage of an aliphatic $CH_3$–O bond. $WO_x$-Com-WC displayed similar activity with more trans-alkylated products like cresols and methyl catechol, presumably due to the introduction of acid sites. However, $W_{1+x}C$-Com-WC exhibited a significant enhancement both in guaiacol conversion and phenol selectivity, reaching 65.3% and 85.3%, respectively. Moreover, with further carburization, WC-Com-WC display a decreased conversion although the phenol selectivity keeps at a high level, in agreement with the previous result of WC@CS. That is to say, the regioselective hydrogenolysis of guaiacol to phenol is depending on the surface reconfiguration between W and C atoms, i.e. the incorporation of suitable C-defects.

**Table 2** Catalytic performance for guaiacol conversion over Com-WC samples modified with different W species.

| Catalyst | Conv. | C6 product selec. /% | | | | | |
|---|---|---|---|---|---|---|---|
| | /% | PhOH | Anisole | Cresols | Benzene | Catechol | Others |
| Com-WC | 7.1 | 51.0 | 0.6 | 9.3 | 0.0 | 2.5 | 36.3 |
| W-Com-WC[a] | 12.6 | 19.1 | 0.0 | 2.0 | 0.0 | 70.3 | 8.6 |
| $W_{1+x}C$-Com-WC[b] | 65.3 | 85.3 | 0.0 | 9.8 | 0.0 | 0.0 | 4.9 |
| WC-Com-WC[c] | 24.0 | 70.9 | 0.0 | 10.6 | 0.0 | 0.0 | 18.5 |
| $WO_3$-Com-WC[d] | 15.5 | 22.5 | 0.0 | 6.9 | 0.0 | 55.8 | 14.8 |

Reaction conditions: weight liquid hourly space velocity (WLHSV) = 3.0 $h^{-1}$, P ($H_2$) = 3.0 MPa, $H_2$/GUA molar ratio = 50, T= 300 °C; [a] pretreated at 450 °C for 4 h at a rate of 5 °C/min under $H_2$; [b] first pretreated from 20 to 450 °C at a rate of 5 °C/min under $H_2$; then 450 to 750 °C at a rate of 1 °C/min for 1 h under 15% $CH_4/H_2$; [c] first pretreated from 20 to 450 °C at a rate of 5 °C/min under $H_2$; then 450 to 750 °C at a rate of 1 °C/min for 6 h under 15%$CH_4/H_2$; [d] pretreated at 450 °C for 4 h at a rate of 5 °C/min under Ar; See Experimental for details.

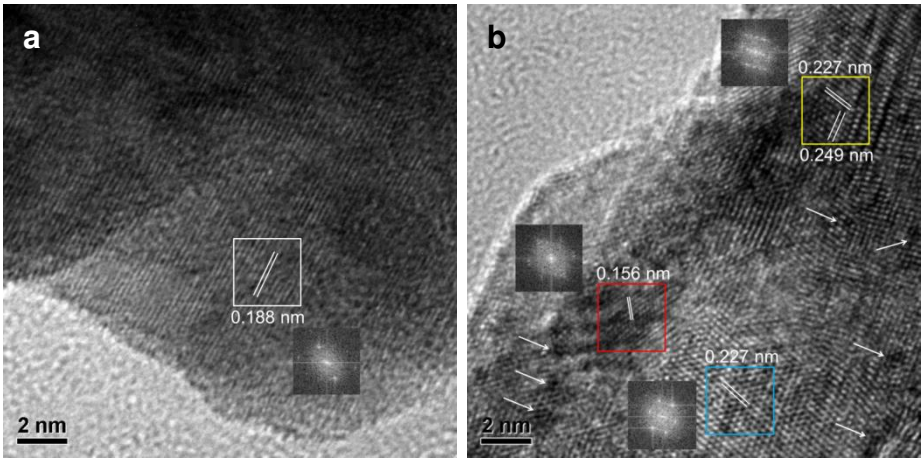


**Fig. 6** HR-TEM images: (a) Com-WC; (b) $W_{1+x}C$-Com-WC.

The effect of surface reconfiguration was further investigated by XPS measurements and chemisorption behavior. As shown in **Fig. S8a**, two typical peaks centred at 31.8 and 33.9 eV are visible on the W 4f profile of the Com-WC, corresponding to the carbidic species of

tungsten. Importantly, a slight negative shift of carbidic W species occurred in $W_{1+x}C$-Com-WC; such a shift might be resulted from the formation of C-defects, affording an electron-rich W species. The binding energy of W-Com-WC was lower than that of $W_{1+x}C$-Com-WC, which can be deconvoluted to carbidic and metallic species. A greater divergence can be observed among these samples from the C 1s profiles in **Fig. S8b**. Com-WC contains two obvious deconvoluted peaks corresponding to the graphitic and carbidic C species. Interestingly, the amount of carbidic C species in the $W_{1+x}C$-Com-WC decreased significantly whereas the graphitic C species are almost unchanged. The carbidic C species of W-Com-WC are almost vanished. These results suggested that C-defects are formed in the $W_{1+x}C$-Com-WC without any metal W segregation, whereas W-Com-WC was coated by metal W species on the surface. Further investigations on CO and $H_2$-TPD have been conducted to provide more evidence on the surface defects dependent activity. In **Fig. S9a**, Com-WC shows weak desorption peak at about 87 °C, at the meantime, the $W_{1+x}C$-Com-WC display similar peaks but instead with bigger and broader peak. Notably, a shoulder peak at higher temperature is more obvious. These observations indicate more C vacancies (or W-terminations) existed on the surface of $W_{1+x}C$-Com-WC. It is worth stressing that the $H_2$-TPD profiles display quite different desorption behavior (**Fig. S9b**). On Com-WC, hydrogen desorbed as a tiny broad peak, in agreement with the previous study [30]. However, when the Com-WC was modified by $W_{1+x}C$ on the surface, hydrogen desorbed as two big and broad signals, indicating the facilitation of hydrogen activation. These results reveal that the reconstruction of surface enriches the formation of hollow carbidic sites and promote the capability for activation of substrate and hydrogen, resulting in a remarkable enhancement in catalytic hydrogenolysis of guaiacol.

3.5 Correlation between phenol production and surface C/W atomic ratio of the catalysts

There is an agreement that photoelectrons escaping depth could be penetrated up to a few nanometers, thus XPS measurements might not truly reflect the composition on the topmost layer. We further explored the outersurface information combined with HS-LEIS, as depicted in **Fig. 7a**. There are only three C, O and W peaks over these samples. It can be found that the peaks of carbon with reconstruction display more obscure than that of Com-WC but the W

and O peaks are almost unchanged. Therefore, C-defect sites were successfully formed after the modification on the surface. The C peak of W-Com-WC is nearly disappeared, suggesting an almost W-terminations on the topmost surface. For exact quantitative analysis, the C/W atomic ratio on the surface was calculated by integrating the relative intensity of W and C from both HS-LEIS and XPS measurements, as indicated in **Fig. 7b**. The C/W atomic ratio of Com-WC by XPS is 1.17:1, closed to the bulk composition of pure WC. With modification of Pt or reconstruction of $W_{1+x}C$ on the surface, the C/W atomic ratio showed a decline to 0.66:1 and 0.44/1, respectively. The results convey that C-defect surfaces were formed under our treatments. On the other hand, W-Com-WC displayed a quite low C/W atomic ratio of 0.15:1, suggesting a surface enrichment of metal W. In contrast, the HS-LEIS results illustrate quite different C/W atomic ratio in comparison with the XPS analysis. The Com-WC possesses higher C/W atomic ratio on the topmost surface, reaching about 16:1, revealing C-terminations on the topmost atomic layer of Com-WC. The ratios in the 1Pt-Com-WC and $W_{1+x}C$-Com-WC rapidly declined to 9.3:1 and 7.2:1 respectively, which is attributed to the etching of the surface carbon atoms, leading to the formation C-defects. Comparatively speaking, W-Com-WC displayed the lowest C/W atomic ratio, obtaining a surface with rich W-terminations.

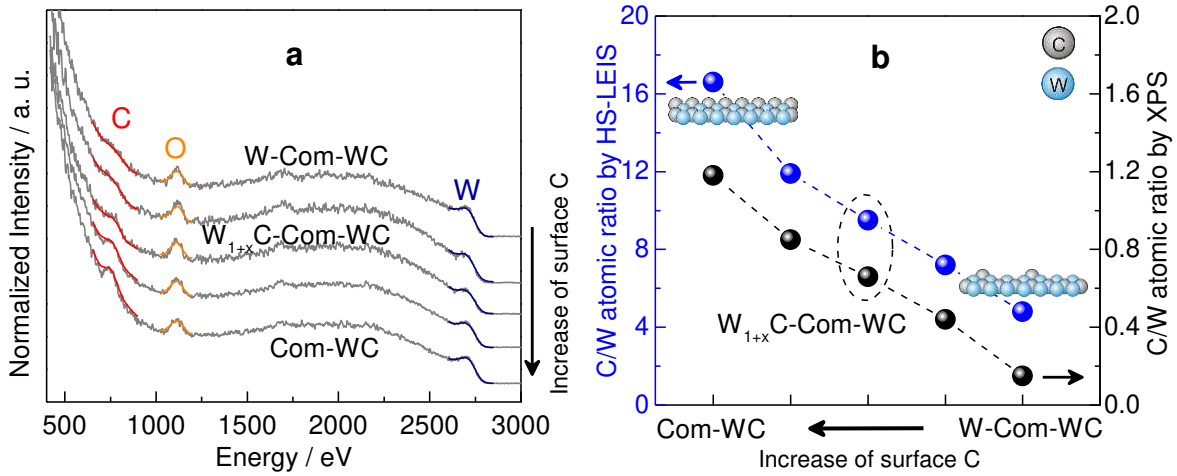


**Fig. 7** C-defect $W_xC$-Com-WC catalysts with increase of surface C: (a) HS-LEIS spectra for the (b) Surface W/C atomic ratio measured by HS-LEIS and XPS.

For quantitative analysis, the phenol STY as a function of the surface C/W atomic ratio is summarized in **Fig. 8**. The phenol STY changed in a volcano-type trend with the increase of

C/W atomic ratio. In low C/W ratio, the surface exposed abundant W-terminations. These surface W atoms displayed an acceptable guaiacol absorption and quite low $H_2$ absorption, resulting in a low phenol production. As the ratio increased, the guaiacol conversion can be significantly promoted, which is contributed to the formation of hollow sites as well as the electronic interaction between W and C atom from the molecules, enhancing the catalytic absorption behaviour. The phenol STY reached the maximum value of 13.6 mmol $g_{cat}^{-1}h^{-1}$ at the C/W ratio of 7.2. Then it would be declined furtherly when the surface was fully occupied by C atoms. These results are in full agreement with the interaction energies of guaiacol and phenol with the slab models, see **Fig 9 and Table 1**. The guaiacol adsorption energies changes from -3.04 eV to -2.11 and to -2.43 respectively on $W_2C\{101\}$, $W_{1.25}C\{110\}$ and $WC\{110\}$. Similar volcano seems to rise from the interaction between phenol and the model surfaces, which interaction energies are -3.33, -1.64 and -2.10 respectively. That is to say, appropriate surface control with rich hollow C-deficient sites benefits the phenol production owing to the optimal textural structure and electronic behaviour. In present, there might be some shortcomings in our study because our samples were not synthesized and characterized under operando conditions due to the unavailability high temperature (over 850 °C) resisting facilities but also because the surface oxidation of carbides is inevitable during preparation. These oxycarbides can introduce some acidic sites or reduce the number of active sites. To exclude the effect, we treated all as-prepared materials with $1\%O_2/99\%N_2$ for 30 min prior to exposure to air to ensure the consistency of oxycarbides.

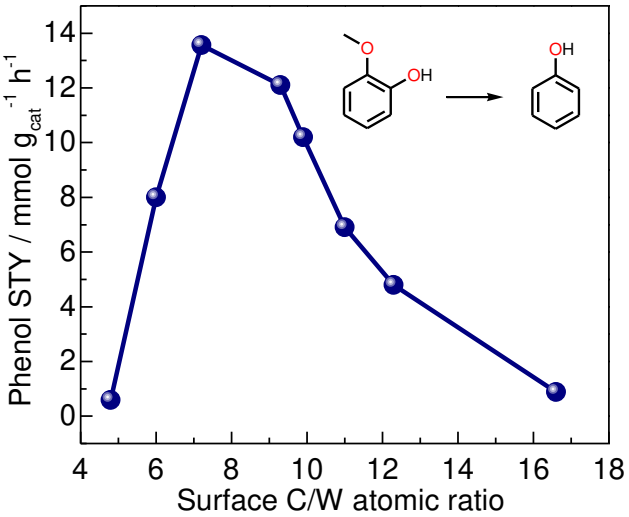


**Fig. 8** Phenol STY for guaiacol hydrogenolysis as a function of the surface C/W atomic ratio

in $W_{1+x}C$-Com-WC catalysts with carburization control.

## 4. Discussion

The textural transformation of carbides involving the insertion of carbon atoms provides a significant redistribution of electron density as well as surface configuration between W and C atoms, altering their catalytic performance. Gong et al. [6] reported that $W_2C$ possessed larger number of states at the Fermi energy than WC by theoretic calculation, in agreement with our calculations. Wang et al. [51] reported a carbon modification method on the metal Ni surface for tuning electronic property of metallic sites, which is highly selective for C–O bond hydrogenolysis reactions. Posada-Pérez and co-workers [52] studied the effect of metal/C ratio in supported molybdenum carbides for $CO_2$ conversion; they found that the increase of the metal/C ratio raised the number of metal centers exposed on the surface, affecting the bonding modes of $CO_2$ and resulting in the formation of $CH_4$ as a side product.

In the present work, the tungsten carbides with well-defined formulation showed appropriate regioselective upon the hydrogenolysis of guaiacol. Our kinetic study also demonstrated that appropriate Ea derives a high selectivity of phenol by hydrogenolysis of aryl C–O bond, particularly on the optimal $W_xC$@CS catalyst. Apparently, the carburization degree and configuration of W and C atoms are particularly crucial in this reaction. In fact, we have shown that both $W_xC$@CS and $W_{1+x}C$-Com-WC possessed abundant crystallographic planes, boundaries, C-defects and stacking faults, as confirmed by the XRD, TEM and HR-TEM measurements. The carburization control and the reconstruction on the surface of Com-WC facilitated tuning the electronic property, which can be further confirmed by XPS. We can see an obvious electron transfer from W to C, during the carburization process or reconstruction treatment, whereas C trapped electrons from W, resulting in electronic richness on C. Indeed, the Bader analysis of atomic charge distribution on the computational models showed an accumulation on the carbons of 1.4, 1.2 and 1.0 electrons respectively for in $W_2C$, $W_{1.25}C$ and WC. Thus, although the number of electrons transferred is lower in absolute value, the total charge per carbon increases considerably with the level of carburisation. The electronic property can be changed subtly when these surface C are partially etching. Our TPD measurements also proved the appropriate activation of both

dihydrogen and substrate play a vital role in transforming guaiacol to phenol.

Consequently, the textural transformation and electronic transfer modulated the catalytic chemisorption behaviour on the condition that an optimal modification on the surface of tungsten carbides, achieving an impressive catalytic performance. The C-vacancies modifies the catalytic properties of the surface affecting the relative stability of intermediates along the guaiacol hydrogenolysis pathway. The clean surface on the $W_2C$ possessed rich C-defects and exposed more W-terminations. These neighbouring W atoms facilitate the absorption of oxygen-containing groups (both $C_{aryl}$–OH and $C_{aryl}$–$OCH_3$) in the guaiacol molecular and intermediates due to the different electronegativities of W and C (2.36 versus 2.55). Indeed, the attraction of oxygen groups by the $W_2C$ surface is clearly represented in **Fig. 9**; the oxygen from the phenol molecule is directly interacting with the surface while on $W_{1.25}C$ and on WC the HO– group remains parallel to the surfaces. The strong interactions result in the cleavage of $C_{aryl}$–OH and $C_{aryl}$–$OCH_3$ bonds rendering the production of anisole and phenol (B and C respectively in **Fig. 9**).

According to the computed energy profile in **Fig. 10**, the anisole pathway is thermodynamically favoured compared to the hydrogenation of $C_{aryl}$–$OCH_3$ group, what could explain the presence of anisole in the products. Further hydrogenation is driven by the formation of phenol (intermediate D) which desorbs (F) or reduces to benzene in an intermediate state between D and G. The phenol generated through intermediate C may further reduce to benzene or desorb. Both pathways, via cleavage of $C_{aryl}$–OH and $C_{aryl}$–$OCH_3$ bonds, lead to downhill profiles, which, together with the favourable stability of benzene and reduced products in gas phase (G), explains the presence of benzene. This process is represented by the diagram in **Fig. 11a**. Further carburisation of the surface leads to $W_XC$@C catalysts which have presented a good catalytic conversion of guaiacol and regioselective towards phenol. Contrarily to $W_2C$ (and WC), this catalysts stabilises the phenol intermediate over the anisole. Both pathways follow a smooth downhill energy profile towards phenol on the surface (D), which explains the good selectivity, see diagram **Fig. 11b**. The complete carburization educes the overall catalytic activity (**Fig. 11c**). The hydrogenolysis of anisole leads to benzene (E), which is less favourable intermediate than phenol (D) produced from the cleavage of the $C_{aryl}$–$OCH_3$ bond, the small energy difference

between these intermediates may limit the selectivity of the hydrogenation process as shown by the experiments.

The surface configuration with careful carburization control is of particularly importance to design catalysts for efficient oriented hydrogenolysis. The results of this study deepen our realization on the structure of tungsten carbides as well as the structure-activity relationship, appealing to wider catalytic applications in the field of hydrogenolysis, surface science and device design.

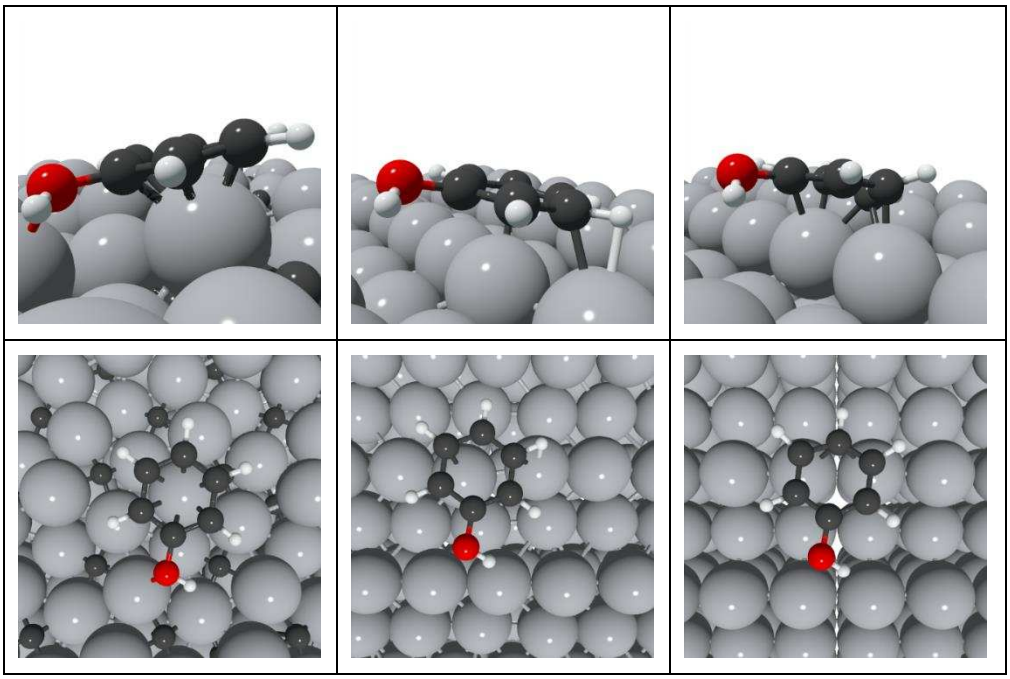

**Fig. 9**. Side and top representations of the most stable phenol configuration adsorbed on $W_2C$, $W_{1.25}C$ and WC from left to right respectively. Colour scheme: clear grey is W, dark grey is C, red is O and white is H.

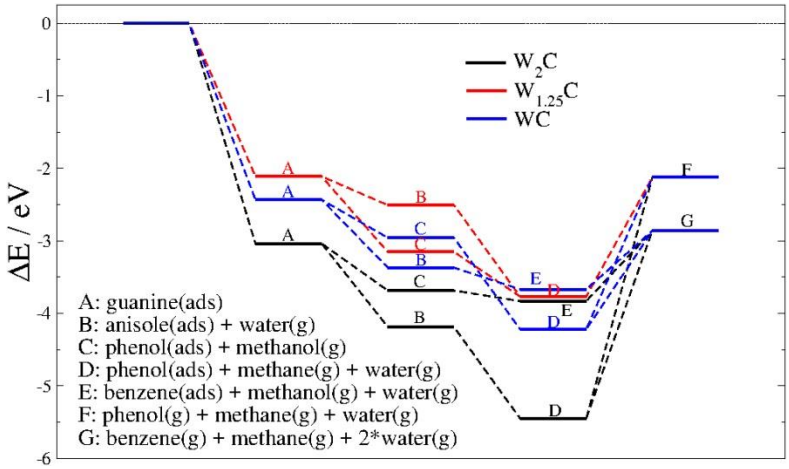

**Fig. 10** Thermodynamic energy profile for guaiacol hydrogenolysis on $W_2C$, $W_{1.25}C$ and WC surfaces (dark, red, and blue lines, respectively).

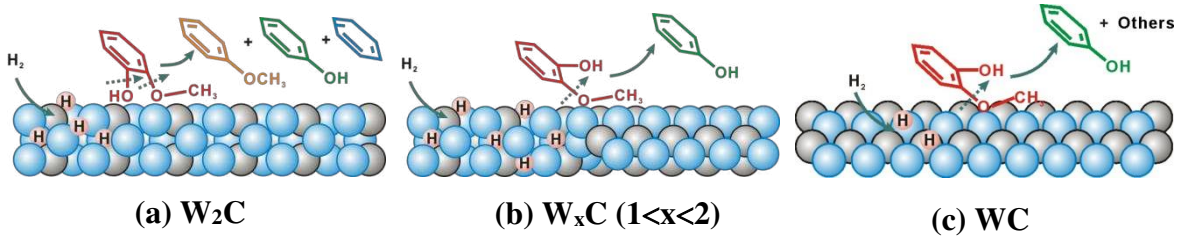


**(a) $W_2C$** **(b) $W_xC$ (1<x<2)** **(c) WC**

**Fig. 11** Plausible scheme for the guaiacol hydrogenolysis on tungsten carbides.

## 5. Conclusions

A series of tungsten carbide catalysts were fabricated by carburization of organic-inorganic hybrid precursors and evaluated for the guaiacol hydrogenolysis. The optimal $W_xC$@CS exhibited high activity and selectivity for the phenol production by direct cleavage of aryl C–O bond. The impressive activity was attributed the appropriate configuration of surface W and C atoms and electronic properties which enriched with grain C-defect sites and boundaries, these were further characterized by detailed textural analysis using XRD, TEM, XPS and HS-LEIS techniques. Controlled experiments by surface reconstruction of pure Com-WC were employed to prove the effect of the surface configuration. The phenol production was directly affected by the changed of the C/W atomic ratio on the surface and showed a volcano-type curve. $W_{1+x}C$-Com-WC possessed the highest phenol STY of 13.6 mmol $g_{cat}^{-1}$ $h^{-1}$, which was attributed to the rich C-defect sites, boundaries and stacking faults. DFT calculations were employed and plausible scheme for guaiacol hydrogenolysis was further proposed to explain the catalytic pathway. This work provides protocols to realize the surface control on tungsten carbides and understand the relationship between structure and catalytic performance, benefiting fundamental studies and rational design of carbide catalysts on hydrogenolysis.

## References

[1] G.S. Ranhotra, A.T. Bell, J.A. Reimer, J. Catal. 108 (1987) 40–49.

[2] E. Furimsky, Appl. Catal. A: Gen. 240 (2003) 1–28.

[3] R.W. Gosselink, D.R. Stellwagen, J.H. Bitter, Angew. Chem. Int. Ed. 125 (2013) 5193–5196.

[4] S.A.W. Hollak, R.W. Gosselink, D.S. van Es, J.H. Bitter, ACS Catal. 3 (2013) 2837–2844.

[5] H. Ren, W.T. Yu, M. Salciccioli, Y. Chen, Y.L. Huang, K. Xiong, D.G. Valchos, J.G. Chen, ChemSusChem 6 (2013) 798–801.

[6] Q.F. Gong, Y. Wang, Q. Hu, J.G. Zhou, R.F. Feng, P.N. Duchesne, P. Zhang, F.J. Chen, N. Han, Y.F. Li, C.H. Jin, Y.G. Li, S.T. Lee, Nat. Commun. 7 (2016) 13216.

[7] A.L. Jongerius, R.W. Gosselink, J. Dijkstra, J.H. Bitter, P.C. A. Bruijnincx, B.M. Weckhuysen, ChemCatChem 5 (2013) 2964–2972.

[8] W.S. Lee, A. Kumar, Z.S. Wang, A. Bhan, ACS Catal. 5(2015) 4104–4114.

[9] J.G. Chen, Chem. Rev. 96 (1996) 1477–1498.

[10] H.H. Hwu, J.G. Chen, Chem. Rev. 105 (2005) 185–212.

[11] J.L. Calais, Adv. Phys. 26 (1977) 847–885.

[12] J.R. Kitchin, J.K. Nørskov, M.A. Barteau, J.G. Chen, Catal. Today 105 (2005) 66–73.

[13] M.G. Quesne, A. Roldan, N.H. de Leeuw, C.R.A. Catlow, Phys. Chem. Chem. Phys. 20 (2018), 6905–6916.

[14] H.H. Fang, J.M. Du, C.C. Tian, J.W. Zheng, X.P. Duan, L.M. Ye, Y.Z. Yuan, Chem. Commun. 53 (2017) 10295–10298.

[15] C.Z. Li, M.Y. Zheng, A.Q. Wang, T. Zhang, Energy Environ. Sci. 2012, 5, 6383–6390.

[16] D.R. Stellwagen, J.H. Bitter, Green Chem. 17 (2015) 582–593.

[17] R. Liu, M. Pang, X.Z. Chen, C. Li, C.J. Xu, C.H. Liang, Catal. Sci. Technol. 7 (2017) 1333–1341.

[18] P.K. Shen, S. Yin, Z. Li, C. Chen, Electrochim. Acta 55 (2010) 7969–974.

[19] A.V. Nikiforov, I.M. Petrushina, E. Christensen, N.V. Alexeev, A.V. Samokhin, N.J. Bjerrum, Int. J. Hydrogen Energy 37 (2012) 18591–18597.

[20] D.V. Esposito, J.G. Chen, Energy Environ. Sci. 4 (2011) 3900–3912.

[21] C.M. Friend, J.G. Serafin, E.K. Baldwin, P.A. Stevens, R.J. Madix, J. Chem. Phys. 87 (1987) 1847–1850.

[22] S.T. Hunt, T. Nimmanwudipong, Y. Roman-Leshkov, Angew. Chem. Int. Ed. 53 (2014) 5131–5136.

[23] J. Lemaître, B. Vidick, B. Delmon, J. Catal. 99 (1986) 415–427.

[24] R.L. Miller, P.T. Wolczanski, A.L. Rheingold, J. Am. Chem. Soc. 115 (1993) 10422–10423.

[25] S.T. Hunt, M. Milina, A.C. Alba-Rubio, C.H. Hendon, J.A. Dumesic, Y. Roman-Leshkov, Science 352(2016) 974–978.

[26] Q.G. Yan, Y.W. Lu, F. To, Y.B. Li, F. Yu, Catal. Sci. Technol. 5 (2015) 3270–3280.

[27] H.B. Wu, B.Y. Xia, L. Yu, X.Y. Yu, X.W. Lou, Nat. Commun. 6 (2015) 6512.

[28] Y.T. Xu, X.F. Xiao, Z.M. Ye, S.L. Zhao, R.A. Shen, C.T. He, J.P. Zhang, Y.D. Li, X.M. Chen, J. Am. Chem. Soc. 139 (2017) 5285−5288.

[29] H.H. Fang, J.W. Zheng, X.L. Luo, J.M. Du, A. Roldan, S. Leoni, Y.Z. Yuan, Appl. Catal. A: Gen. 529 (2017) 20–31.

[30] A.G. Sergeev, J.F. Hartwig, Science 332 (2011) 439–443.

[31] A.J. Ragauskas, G.T. Beckham, M.J. Biddy, R. Chandra, F. Chen, M.F. Davis, B.H. Davison, R.A. Dixon, P. Gilna, M. Keller, P. Langan, A.K. Naskar, J.N. Saddler, T.J. Tschaplinski, G.A. Tuskan, C.E. Wyman, Science 344 (2014) 709.

[32] J.R. Kitchin, J.K. Nørskov, M.A. Barteau, J.G. Chen, J. Chem. Phys. 120 (2004) 10240–10246.

[33] M.P. Humbert, C.A. Menning, J.G. Chen, J. Catal. 271 (2010) 132–139.

[34] J.P. Perdew, A. Ruzsinszky, G.I. Csonka, O.A. Vydrov, G.E. Scuseria, L.A. Constantin, X.L. Zhou, K. Burke, Phys. Rev. Lett. 100 (2008) 136406.

[35] N.D. Mermin, Phys. Rev. 137 (1965) A1441.

[36] G. Kresse, D. Joubert, Phys. Rev. 59 (1999) 1758.

[37] S. Grimme, J. Antony, S. Ehrlich, H. Krieg, J. Chem. Phys. 132, (2010) 154104.

[38] D. Santos-Carballal, A. Roldan, R. Grau-Crespo, N.H. de Leeuw, Phys. Chem. Chem. Phys., 16 (2014) 21082−21097.

[39] N.Y. Dzade , A. Roldan, N.H. de Leeuw, Phys. Chem. Chem. Phys., 16, (2014) 15444–15456.

[40] D. Santos-Carballal, A. Roldan, R. Grau-Crespo, N.H. de Leeuw, Phys. Rev. 91 (2015)

195106.

[41] H.J. Monkhorst, J.D. Pack, Phys. Rev. B 13 (1976) 5188.

[42] P.E. Blöchl, O. Jepsen, O.K. Andersen, Phys. Rev. B 49 (1994) 16223.

[43] T. Epicier, J. Dubois, C. Esnouf, G. Fantozzi, P. Convert, Acta Metallurgica, 8 (1988) 1903–1921.

[44] K.D. Litasov, A. Shatskiy, Y.W. Fei, A. Suzuki, E. Ohtani, K. Funakoshi, J. Appl. Phys., 108 (2010) 053513.

[45] P.W. Tasker, J. Phys. C: Solid State Phys, 12 (1979) 4977.

[46] G.W. Watson, E.T. Kelsey, N.H. de Leeuw, D.J. Harris, S.C. Parker, J. Chem. Soc., Faraday Trans., 92 (1996) 433–438.

[47] T. Nimmanwudipong, C. Aydin, J. Lu, R.C. Runnebaum, K.C. Brodwater, N.D. Browning, D.E. Block, B.C. Gates, Catal. Lett. 142 (2012) 1190–1196.

[48] Y. Nakagawa, M. Ishikawa, M. Tamura, K. Tomishige, Green Chem. 16 (2014) 2197–2203.

[49] W.S. Lee, Z. Wang, R.J. Wu, A. Bhan, J. Catal. 319 (2014) 44–53.

[50] J.R. Kitchin, J.K. Nørskov, M.A. Barteau, J.G. Chen, Phys. Rev. Lett. 93 (2004) 156801.

[51] M. Wang, X.C. Zhang, H.J. Li, J.M. Lu, M.J. Liu, F. Wang, ACS Catal. 8 (2018) 1614–1620.

[52] S. Posada-Pérez, P.J. Ramírez, J. Evans, F. Viñes, P. Liu, F. Illas, J.A. Rodriguez, J. Am. Chem. Soc. 138 (2016) 8269−8278.